Intrinsic heat treatment induced graded surficial microstructure and tribological properties of selective laser melted titanium

Nan Kang[1]
State Key Laboratory of Solidification Processing, Northwestern Polytechnical University, Xi'an Shaanxi 710072, PR China
Key Laboratory of Metal High Performance Additive Manufacturing and Innovative Design, MIIT China, Northwestern Polytechnical University, Xi'an, China
e-mail: nan.kang@nwpu.edu.cn

Nicolas Coniglio
Laboratory of Mechanics, Surface and Materials Processing, Arts et Métiers Paristech
2 cours des Arts et Métiers, 13617 Aix-en-Provence, France
e-mail: Nicolas.CONIGLIO@ensam.eu

Yang Cao
State Key Laboratory of Solidification Processing, Northwestern Polytechnical University, Xi'an Shaanxi 710072, PR China
Key Laboratory of Metal High Performance Additive Manufacturing and Innovative Design, MIIT China, Northwestern Polytechnical University, Xi'an, China
e-mail: cy94@mail.nwpu.edu.cn

Chunling Zhao[1]
AECC Hunan Aviation Powerplant research institute, Zhuzhou, Hunan, China
e-mail: capi@608.163.net

Mohamed El Masnori
Laboratory of Mechanics, Surface and Materials Processing, Arts et Métiers Paristech
2 cours des Arts et Métiers, 13617 Aix-en-Provence, France
Department of Industrial and Systems Engineering, Texas A&M University, 3131 TAMU, College Station, TX 77843, USA
e-mail:Mohamed.elmansori@ensam.eu

Yu Zhao
AECC Hunan Aviation Powerplant research institute, Zhuzhou, Hunan, China
e-mail: 2632006321@qq.com

Xin Lin
State Key Laboratory of Solidification Processing, Northwestern Polytechnical University, Xi'an Shaanxi 710072, PR China
Key Laboratory of Metal High Performance Additive Manufacturing and Innovative Design, MIIT China, Northwestern Polytechnical University, Xi'an, China
e-mail: xlin@nwpu.edu.cn

Christian Coddet
ICB UMR 6303, CNRS, Univ. Bourgogne Franche-Comté, UTBM, F-90010 Belfort, France
e-mail: christian.coddet@wanadoo.fr

[1] Corresponding author information can be added as a footnote.

ABSTRACT

In the course of the selective laser melting (SLM) process, the part is built layer by layer involving partial re-melting/heating of the previous layer, called as intrinsic heat treatment. Therefore, superficial properties of as-built parts are somewhat different from that of the inside of the part. In this work, the nano-tribological behavior of commercial pure Ti (CP-Ti) sample built using SLM was investigated considering the near-surface regions with focus on the effect of intrinsic heat treatment. Microstructure and nano- testing allow identifying specific sliding behaviors in three attitude regions: (I) surface (0 to 50 µm); (II) subsurface (50 to 200 µm); (III) inner-part (below 200 µm). The average hardness drops slightly when moving from Regions I and II (3.35 GPa) to Region III (3.09 GPa). The friction coefficient (COF) values vary from 0.18 to 0.45 for all three regions, and the region III presents highest worn trace width of 5.8 µm. Regions (I) and (III) promote a stick-and-slip behavior while sliding is smooth and continuous in Region (II). This gradient microstructural characterization enables associating the behavior of region (II) to large-sized lath martensite α' morphology, which is different from the region I and III with finer microstructure. A FEA thermal model suggests that the existence of the three identified regions is the consequence of the intrinsic heat treatment induced by the SLM process, in which the re-melting/heating and recrystallization have been considered as the main reasons for microstructure coarsening and refinement between region I and II, region II and III, respectively.

Keywords: Selective laser melting; Intrinsic heat treatment; Titanium; Microstructural gradient; Nano-tribology.

1. Introduction

Fabricating complex-shaped titanium parts is challenging when using traditional processes but is nowadays facilitated by additive manufacturing processes, such as selective laser melting (SLM). SLM is a powder-bed laser fusion additive manufacturing process that is convenient to produce small size components with complex geometries,

such as lattice or porous structures [1-3]. This merit brings great potential application of SLM technology in medical and biological industries for custom-made metallic implant production. Commercial pure Ti (CP-Ti) is commonly used for manufacturing biomedical prostheses given its low density, low elastic modulus, high strength, good corrosion resistance, biocompatibility and nontoxicity [4].

In general, the design of Ti implants, among several requirements such as corrosion resistance or specific roughness, needs to take into account the surface wear behavior when sliding against body or artificial counterparts. The aim of course is to attain minimum friction force with low wear debris. Thus, the wear behavior of SLM processed CP-Ti components has already been the subject of a number of studies [5-9] and it was reported that SLM processed CP-Ti exhibits higher wear resistance than the casted one, which is attributed to the high cooling rate inducing fine microstructure and metastable phase. Meanwhile, these previous works focused mainly on the macro or micro wear behaviors with loads up to dozen Newton and only few work considered the nano-scale superficial wear properties [9], which is known to be quite different from micro and macro wear [8,9].

In addition, as the common shortages of layer by layer additive manufactured components, the as-processed part always possesses the heterogeneous microstructure [10, 11] with a subsequent anisotropic mechanical behavior [12-14]. Among them, one nonnegligible point is the gradient surface structure and properties [15, 16], which is mainly due to the numerous cycles of heating and cooling undergone by the material during the laying down of each constitutive layer [17]. This kind of *in-situ* heat-treating

may also induce some beneficial effects on component production, such as stress relaxation or build-up, solid-state phase transition and precipitation. Therefore, this important *in-situ* heat-treating is called as intrinsic heat treatment for further investigation [18].

Therefore, in the present work, the CP-Ti sample was manufactured using SLM with optimized process parameters. Then, the microstructure was investigated using X-ray diffraction (XRD), scanning electron microscopy (SEM), electron backscatter diffraction (EBSD) and transmission electron microscopy (TEM). Then, SLM processed CP-Ti specimen was characterized by nano-wear testing on cross-section at various depths and the tribological behavior was then associated to microstructural features and thermal history.

2. Experimental conditions

2.1 Manufacturing parameters

The CP-Ti powder was manufactured by gas-atomization from Ti grade 1 raw material. A mean particle size of 41.7 µm was measured by laser light scattering, shown in Fig. 1. Parallelepiped sample 30 x 10 x 10 mm^3 was printed with a SLM 250 machine (MCPHEK Tooling GmbH, Germany) equipped with an Nd-YAG fiber laser (1.064 µm wavelength). Optimum process parameters (40 µm diameter spot size; 1250 $mm \cdot s^{-1}$ scanning speed; 175 W laser power, 50 µm layer thickness) were determined during a previous study [12]. A zigzag manufacturing pattern, with a hatch distance of 110 µm and a scanning rotation of 90° between successive layers was selected.

Eq. 1 gives the linear (E_L) energy density actually introduced into the material

$$E_L = \eta \frac{q}{v} = 0.11\ J \cdot mm^{-1}$$ Equation (1)

where q is the laser beam power (175 W), v the scanning speed (1250 mm·s^{-1}), and η an efficiency coefficient. For Ti alloys and a Nd:YAG SLM process this coefficient was determined as 0.77 [19].

2.2 Microstructural characterization

Prior to mechanical testing and metallographic observation, cross-section of the specimen was cut, ground, and polished according to the standard metallographic procedures, 200#, 400#, 1000#, 2000# and 4000# grit papers for 2 min and then OP-S polishing (0.025 μm) for 4 min.

The phase of SLM processed sample was characterized by XRD with scanning speed about of 1º/min. Microstructure was mainly observed using SEM and EBSD. Prior to observation, polished sample was etched in a 15 ml HNO_3, 5 ml HF and 80 ml H_2O solution. Observation was performed in $2 \cdot 10^{-3}$ Pa vacuum at 15.0 kV accelerating voltage and 10.0 mm working distance on a JEOL JSM-7001F fitted with a HKL Nordlys camera (Oxford Instruments) controlled by the CHANNEL5 software suite. TEM (FEI-Talos F200X) was also performed on some samples prepared by twin jet electrolytic thinning.

2.3 Finite element modeling method

A 3D finite element analysis (FEA) model was developed by software package ABAQUS, which has been verified and validated in our previous work by experimental method in case of SLM processed Al alloys [20]. Fig. 2 shows the geometry of the model, which includes the substrate plate with size of 5 mm × 5 mm × 2 mm and the laser deposited region with size of 1 mm×1 mm, a total of 10 layers height (0.5 mm). The

element size of deposited pass is set as 0.5 µm × 0.5 µm × 0.5 µm. The element of remaining parts is properly enlarged for saving the computing costs and ensuring the required accuracy. The temperature-dependent physic properties are adopted from the work of X.F. Lu et al. in case of similar chemical composition of Ti6Al4V [21]. The Gaussian moving heat source (as described in (Eq. 2) with reciprocating scanning strategy was loaded by subroutine DFLUX.

$$q(x,y,z,t) = \frac{6\sqrt{3}Q}{abc\pi\sqrt{\pi}} \exp\left(-\frac{3(x-v_x t)^2}{a^2} - \frac{3(y-v_y t)^2}{b^2} - \frac{3(z-v_z t)^2}{c^2}\right) \quad \text{Equation (2)}$$

where a, b, c are the semi-axes of the ellipsoid in x, y, z direction respectively.

2.4 Mechanical testing

Mechanical properties of the SLM-produced specimens were investigated in cross sections by nano-indentation and nano-wear measurements using a Morphoscan apparatus from Michalex Tribometrix. A Fused Silica reference sample (E=69.4 GPa; v=0.17) was used for calibration before conducting the nano-indentation tests that were performed using a Berkovich diamond tip (E=1141 GPa; v=0.07) with a constant strain rate of 0.05 s^{-1} for loading and unloading and with a maximum load of 50 mN. Elastic modulus and hardness were calculated using the Oliver and Pharr analysis considering the Poisson coefficient of CP-Ti as 0.32.

Nano-wear testing was performed with a 10 µm-radius spherical indenter under a 50 mN load at a displacement rate of 2 µm·s^{-1}, with a reciprocal linear sliding distance of 200 µm. The 50 mN load secures a plastic friction behavior without excessive stripping and extensive plastic flow [20]. Testing was performed at several sub-surface depths on polished cross-section.

3. Results

3.1 Microstructure

The XRD results are shown in Fig. 3, it can be seen that the diffraction peaks slightly shift to the smaller diffraction angles versus standard diffraction peaks of *hcp* α-Ti, indicating the presence of martensitic α' phase [5]. The α' is known to precipitate from prior β grains at high cooling rates [7, 13, 22] and the presence of this dense *hcp* α' martensite in our SLM produced CP-Ti is in agreement with previous findings [7, 9, 10-12].

Fig. 4 shows the all Euler mapping of the microstructure observed on a cross section parallel to the building direction. Three regions can be distinguished along distance from top surface and referred to as Region I (0-50 µm depth), Region II (50-200 µm depth) and Region III (>200 µm depth). Region I corresponds to the last deposited layer. The 4 ±2 µm width of the α'-laths agrees with observation made on SLM Ti6Al4V produced with a slightly faster scanning speed (1500 $mm \cdot s^{-1}$) [13]. Compared to Region I, the subsurface Region II consists in a coarser microstructure with lath and acicular grain morphologies (as indicated by arrows in Fig. 4). The lath α' martensite grains are 5 to 10 µm wide and 50 to 80 µm long. The zig-zag scanning mode induces no obvious preferred orientation of α grain in the entire sample. During SLM of Ti alloys, the orientation of α grain is affected by the prior β grain during the solid-state phase transition, which is determined as one kind of shear phase transition with lath or acicular morphology. The crystalline relationship between α and β will be presented in the texture analysis (Fig. 5) and our previous work [16]. Meanwhile, the inner Region III

exhibits an ultra-fine microstructure. This microstructure gradient is attributed to the effect of an intrinsic heat treatment during the SLM process, leading to the recrystallization [17, 23]. More detailed discussion will be given combining the TEM observation.

EBSD analyses attempt to determine the statistical distribution in grain boundary misorientations and crystallographic textures (Fig. 5). As observed in Fig. 5a and b, the misorientation measurements reveal two dominant values of 60 and 63° in Regions I and II but only one (60°) in Region III. Among the different α' variants that form in each parent β grain, it has been observed by other researchers [10] in SLM processed Ti6Al4V that α' clusters misoriented 63.26° apart around the $\langle \bar{1}055\bar{3} \rangle$ (type 4) or 60° around $\langle 11\bar{2}0 \rangle$ (Type 2) are predominantly formed. Our measurements suggest that intrinsic heat-treating induces a transition from type 4 to type 2, leading to only type 2 in Region III of CP-Ti. Additionally, it can be seen that the prior β Ti grains present columnar morphology at region II and III, which is attributed the high temperature gradient along building direction during the melting and re-melting procedures. The high maximum texture intensity value of 4.34 in the ⟨0001⟩ direction of the *hcp* Ti-crystals within one columnar β grain (Fig. 5c) indicates a trend to local texturation in Region II.

TEM analyses on sample cross section (Fig. 6) reveal inhomogeneous features through the different regions. The surface Region I (Fig. 6a and b) exhibits a lath martensite α', in agreement with other works [5, 13], in which wide (200-300 nm) and narrow (50-150 nm) sub-grains appear alternatively. The sub-surface (Region II in Fig. 6c) is composed of lath-shaped α' with much larger size (over 1 µm) as already observed by

EBSD (Fig. 4a). Moreover, the high density of dislocation can be observed inside α' grains. The inner Region III shows a quite different morphology consisting of irregular α' grain with lath-shaped α' sub-grains (Fig. 6d). Higher magnification (Fig. 6e) allows identifying two morphologies: narrow (a few nanometers) and wide (hundreds of nanometers) laths. According to the work of Zhong et al. [24], this twinning structure would be induced by thermal cycling (annealing) that firstly lead to a recrystallization of the α' phase following by dislocation enhanced movements as schematically illustrated in Fig. 6f.

3.2 Local mechanical properties

The macro mechanical properties of SLM processed CP-Ti can be found in our previous work [12]. Thus, nano-scale mechanical properties were measured on cross-section across Regions I, II and III from the top surface to 800 µm depth with a 25 µm-spacing between indents in this study (Fig. 7). The average values of Young's modulus and hardness are respectively 126 GPa (standard deviation of 8 GPa) and 3.2 GPa (standard deviation of 0.2 GPa). These values are in line with other works [5, 9]. Meanwhile, a small drop in the average hardness was observed when moving from Regions I and II (3.35 GPa) to Region III (3.09 GPa). It is related to the solid-state phase transition as supported by EBSD results: relatively coarsened lath-shaped → refined acicular-shaped martensitic → refined zigzag-structured martensite [25]. Moreover, the formation of {2-1-10} twinning system in hcp-α' Ti allows accommodating shape strain, assisting shear strain and lattice unchanging strain .

It is generally considered that wear resistance of a material is related to its ability to resist transition from elastic strain to failure at the nanometer scale, which is indicated by H/E and H^3/E^2 ratios [9]. Thus, high hardness and low Young's modulus indicate high wear resistance. The H^3/E^2 ratio, referred to as yield pressure, indicates resistance to plastic deformation by limiting gradual removal of the material. Present corresponding values are, for H/E 0.026 and 0.024, and, for H^3/E^2 0.0023 and 0.0018, respectively for Regions II and (I and III).

The friction coefficient (μ, COF) of the diamond tip is initially calculated for each wear trace as the ratio between the average value of normal (N) and tangential (T) forces during the wear movement. Those calculated average values from three measurements have been performed at each depth vary from 0.18 to 0.45 (seen in Fig. 8 (a)), which agrees with previous works [22, 26]. While COF appears independent from the tested region, it is not the case for the dynamic behavior, with intermittent sliding in Regions I and III and smooth continuous sliding in Region II. This result can be seen in Fig. 8 (b) that the error bars of region II are much smaller than that of region I and III.

Differences in dynamic behavior may be revealed considering the evolution of the COF with time during wear testing. A COF increment is observed here to be associated to the stopping of the indenter movement and to an increase in the tangential force. As shown in Fig. 9a, the continuous advancing mode in Region II is different from the stick-and-slip advancing mode in Regions I and III. The intermittent sliding in Regions I and III appears similar to the macro-wear behavior of SLM processed Ti [5, 27]. In nano-scale condition, this behavior is not related to the surface morphology (roughness R_a smaller

than 0.2 µm, which is too small for mechanical anchoring) nor to cold welding effect (sliding speed of 2 µm·s^{-1} which is too slow for high local heat generation). Therefore, it may be inferred that intermittent sliding is due to material piling up ahead the indent until it is suddenly expelled, releasing the indent for the advancing movement [22]. This difference of Regions I and III versus Region II could thus well originate from a relationship between the grain size and the diamond tip radius. Indeed, while Regions I and III have α laths smaller than the wear trace width, Region II has larger grain size with fewer grain boundaries, which seems to impede dislocations slips. The subsequent continuous plastic deformation promotes a sliding behavior with little fluctuation.

Observation by SEM (Fig. 9b) revealed different post-wear features for the different Regions. It can be seen that the widths of wear trace in Region III and I (5.8 µm and 4 µm) are larger than that of Region II (3 µm), which indicates a relative weak wear resistance of Region III and I, which also conforms well the hardness results in Fig. 7. Moreover, wear traces in Regions I and III display extrusions of matter on the sides of the groove and delamination at the bottom of the groove. On the contrary, wear trace in Region II displays no extrusion on the groove sides and ploughing at the bottom. Delamination observed in Regions I and III may be caused by the shear of void defects and subsequent propagation of cracks from subsurface to surface [27]. Dislocation density is high because martensitic transformation is associated to very high dislocation content and transformation-induced stress in the material. The penetration *p* of the indenter (radius R = 10 µm) is of average value around 400 nm, the normal stress for a force *N* of 50 mN is given by (Eq. 3):

$$\sigma_N = \frac{F}{A} = \frac{F}{\pi(Rp - p^2)} = 4.2\ GPa$$ Equation (3)

For a COF in the range of 0.18-0.45, the tangential stress σ_T is in the range of 0.75-1.87 GPa ($\sigma_T = COF \cdot \sigma_N$). Drag stress ($\sigma_f$) in titanium being in the 95-200 MPa range [28], there may be therefore dislocation movements and piling up ahead of the indenter. Thus, considering the advancing behavior of the diamond tip during the nano-wear test, a nano-wear mechanism is proposed for which a necessary and sufficient control condition could be the lath size of the α' martensitic phase.

The delamination theory suggests that the thickness of delaminated sheet (*h*) is related to the shear modulus (*G*), Burgers vector (*b*), Poisson's coefficient (ν), and drag stress (σ_f) according to the relationship [26], Eq. 4:

$$h = \frac{G \cdot b}{4 \cdot \pi \cdot (1-\nu) \cdot \sigma_f}$$ Equation (4)

where G is related to the measured Young modulus E, Eq. 5 :

$$G = \frac{E}{2 \cdot (1+\nu)}$$ Equation (5)

Considering *E*=123 GPa, ν=0.32, σ_f = 95 MPa, and *b* = 3 Å [29], the thickness h of delaminated sheet is 17 nm. Comparing this value to the grain size observed by TEM (Fig. 6), this size is of the order of magnitude of the sub-grains in Regions I and III but two orders of magnitude smaller than the sub-grain size in Region II. Among the two deformation modes observed in SLMed Ti (sliding of slip band inside grains and of shear band at grain boundary), the present work suggests that the Regions I and III are sensitive subgrain boundary fracture.

From the observation it may be concluded that among the various possible wear mechanisms [8, 27], the most likely to occur here is ploughing for Region II and cutting for Regions I and III. These wear mechanisms are in good agreement with the observation in other works [5, 7].

4. Discussion

The SLM process involves highly localized heat input during very short time resulting in complex microstructure. Therefore, understanding the microstructure of SLM processed materials requires the knowledge of thermal field within the sample. Based on that, the FEA calculated results with 10 deposited layers are shown in Fig. 10. It can be seen that as the deposited layer number increases, the thermal field presents a slight increment of peak and base temperatures as the result of thermal accumulation. One thermal data picking point was chosen at the center of first deposited layer, which is indicated by star in Fig. 10. The thermal history (seen from Fig. 10) indicates that a clear thermal cycling phenomenon appears during SLM procedure. Seen from the data of picking point, in cycling 1 (C1), the powder was heated up over melting temperature and then suffered the laser scanning neighbor line-line interaction. As the laser beam moved away, the temperature decreased rapidly. Along the 2^{nd} deposition (C2), the temperature of picking point was again heated up to very high temperature and cooling (remeling). With periodic deposition and scanning, the thermal cycling can be observed from about 8 layers (C1-C8). In C8 cycling, the data picking point was only heated to about 600 K, after that, the thermal cycling is negligible. It should be noted that the peak temperature of C5 is about 1100K, which approaches to the α-β transition

temperature. Thus, the intrinsic heat treatment induced gradient structure appears with C1 (No.1 layer: 50μm)-RI, C2/4(No.2-4 layer: 50-200μm)-RII, after C5-RIII, which are well coincided with experimental results. Apart from as-deposited Region I, in order to explain the microstructural evolution between region II and region III, one possible mechanism is discussed as follow:

Boundary splitting recrystallization: Given to the high cooling rate, the dislocation density and residual stress of SLM processed component are much higher than that of traditional casted one (see in Fig. 6). During the intrinsic heat treatment of SLM process, the previous deposited layers are heated for several times like a cycling heat treatment (see in Fig. 10). According to the work of Weiss et al. [30] and Sabban et al. [31], the heating and cooling between β and α leads to the dislocation arrangement or shear bonds inside the α grain with a result of subgrain boundary. Then, after several heating/cooling cycles, the large sized α grain will be separated into several small sized α grians, or twining structure (see in Fig. 6d). In this mechanism, both the high dislocation density and residual shear stress have been considered as source for subgrain boundary formation. However, unfortunately, the real reason behind this microstructure refinement is difficult to be directly determined, because of ultra-high heating and cooling rates and small melting pool sizes during SLM.

Therefore, the following assumption is proposed. Region I corresponds to an as-solidified fine α'-martensite microstructure with high cooling rate during solidification. In Region II, the re-melting and heating make the α'-martensite grow, inducing the formation of long laths morphology. Particularly, partial remelting at the upside of

region II enhances growth and regrowth from prior grains across the layers. In region III, the boundary splitting recrystallization induces the large sized α' refinement. Thus, the observed grain refinement combines to a drop in hardness, which suggests some dislocation movements associated to the thermal induced recrystallization and twining structure.

5. Conclusion

Microstructure and nano-tribological behavior of SLM processed CP-Ti were investigated in the surface and sub-surface regions of the sample. Microstructural analysis shows a continuous microstructure gradient from the surface, subsurface and inner regions. EBSD and TEM analyses demonstrate that the occurrence of the $\beta \rightarrow \alpha'$ transition and thermal field modeling indicates that the thermal cycling during SLM induces the solid-state phase transition and grain coarsening and refinement. This microstructure gradient results in two different nano-wear mechanisms with either continuous or intermittent advancing movements of the indenter. Material removal during sliding changes from cutting (Regions I and III) to ploughing (Region II) leading to reduced wear rate and debris formation in Region II.

Acknowledgment

This work was supported by the National Key R&D Program of China [Grant No. 2016YFB1100100] and Fundamental Research Funds for the Central Universities [Grant No, 31020180QD130] and Aero Engine Corporation of China [Grant No. HFZL2019CXY019].

References

[1] Kruth J.P., Leu M.C., Nakagawa T., 1998, “Progress in Additive Manufacturing and Rapid Prototyping,” CIRP Ann. - Manuf. Technol. 47, pp. 525-540.

[2] Olakanmi E.O., Cochrane R.F., Dalgarno K.W., 2015, “A review on selective laser sintering/melting (SLS/SLM) of aluminium alloy powders: Processing, microstructure, and properties,” Prog. Mater. Sci. 74, pp. 401-477.

[3] Gusarov A.V., Yadroitsev I., Bertrand P., Smurov I., 2007, “Heat transfer modelling and stability analysis of selective laser melting,” Appl. Surf. Sci. 254, pp 975-979.

[4] Ezugwu E.O., Wang Z.M., 1997, “Titanium alloys and their machinability—a review,” J. Mater. Process. Technol. 68, pp. 262-274.

[5] Gu D., Hagedorn Y.C., Meiners W., Meng G., Batista R.J.S., Wissenbach K., Poprawe R., 2012, “Densification behavior, microstructure evolution, and wear performance of selective laser melting processed commercially pure titanium,” Acta Mater. 60, pp. 3849-3860.

[6] Fischer P., Romano V., Weber H.P., Karapatis N.P., Boillat E., Glardon R., 2003, “Sintering of commercially pure titanium powder with a Nd:YAG laser source,” Acta Mater. 51, pp. 1651-1662.

[7] Attar H., Prashanth K.G., Chaubey A.K., Calin M., Zhang L.C., Scudino S., Eckert J., 2015, “Comparison of wear properties of commercially pure titanium prepared by selective laser melting and casting processes,” Mater. Lett. 142, pp. 38-41.

[8] Deuis R.L., Subramanian C., Yellupb J.M., 1997, “Dry sliding wear of aluminium composite-a review,” Compos. Sci. Technol. 57, pp. 415–435.

[9] Attar H., Calin M., Zhang L.C., Scudino S., Eckert J., 2014, “Manufacture by selective laser melting and mechanical behavior of commercially pure titanium,” Mater. Sci. Eng. A., 593, pp. 170-177.

[10] Simonelli M., Tse Y.Y., Tuck C., 2014, “On the Texture Formation of Selective Laser Melted Ti-6Al-4V,”, Met. Mat. Trans. 45A, pp. 2863-2872.

[11] Thijs L., Verhaeghe F., Craeghs T., Van Humbeeck J., Kruth J.P., 2010 “A study of the microstructural evolution during selective laser melting of Ti–6Al–4V,” Acta Mater., 58, pp. 3303-3312.

[12] Kang N., Yuan H., Coddet P., Ren Z., Bernage C., Liao H., Coddet C., 2017, “On the texture, phase and tensile properties of commercially pure Ti produced via selective laser melting assisted by static magnetic field,” Mater. Sci. Eng. C. 70, pp. 405-407.

[13] Ren Y.M., Lin X., Fu X., Tan H., Chen J., Huang W.D., 2017, “Microstructure and deformation behavior of Ti-6Al-4V alloy by high-power laser solid forming,” Acta Mater., 132, pp. 82-95.

[14] Pesach A., Tiferet E., Vogel S.C., Chonin M., Diskin A., Zilberman L., Rivin O., Yeheskel O., Caspi E.N., 2018, “Texture analysis of additively manufactured Ti-6Al-4V using neutron diffraction,” Addit. Manuf. 23, pp. 394-401.

[15] Liu Y.J., Liu Z., Jiang Y., Wang G.W., Yang Y., Zhang L.C., 2018, “Gradient in microstructure and mechanical property of selective laser melted AlSi10Mg,” J. Alloys Compds 735, pp.1414-1421.

[16] Kang N., Lin X., El Mansori M., Wang Q.Z., Lu J.L., Coddet C., Huang W.D., 2020, “On the effect of the thermal cycle during the directed energy deposition application to the

in-situ production of a Ti-Mo alloy functionally graded structure," Addit. Manuf. 31, 100911.

[17] Krakhmalev P., Yadroitsava I., Fredriksson G., Yadroitsev I., 2015, "In situ heat treatment in selective laser melted martensitic AISI 420 stainless steels," Mater. Des. 87, pp. 380-385.

[18] Damon J., Koch R., Kaiser D., Graf G., Dietrich S., Schulze V., 2019, "Process development and impact of intrinsic heat treatment on the mechanical performance of selective laser melted AISI 4140," Addit. Manuf., 28, pp275-284.

[19] Kruth J.P., Wang X., Laoui T., Froyen L., 2003, "Lasers and materials in selective laser sintering," Assembly Automation, 23, pp. 357-371.

[20] Cao Y., 2020, "Numerical modeling of thermo-mechanical coupling behaviours of selective laser melting in AlSi10Mg," master dissertation, Northwestern Polytechnical University, Xi'an, China.

[21] Lu X., Lin X., Chiumenti M., Cervera M., Li J., Ma L., Wei L., Hu Y., Huang W., 2018, "Finite element analysis and experimental validation of the thermomechanical behavior in laser solid forming of Ti-6Al-4V," Addit. Manuf. 21, pp394-401.

[22] Kang N., El Mansori M., Coniglio N., Coddet C., 2018, "Nano-wear-induced behavior of selective laser melting commercial pure titanium," Procedia Manuf., 26, pp. 1034-1040.

[23] Mercelis P., Kruth J. P., 2006, "Residual stresses in selective laser sintering and selective laser melting," Rapid Prototyping J., 12, pp. 254-265.

[24] Zhong H.Z., Zhang X.Y., Wang S.X., Gu J.F., 2018, “Examination of the twinning activity in additively manufactured Ti-6Al-4V,” Mater. Des., 144, pp. 14-24.

[25] Verhaeghe F., Craeghs T., Heulens J., Pandelaers L., 2009, “A pragmatic model for selective laser melting with evaporation,” Acta Mater., 57, pp. 6006-6012.

[26] Kang N., Coddet P., Liu Q., Liao H.L., Coddet C., 2016, “In-situ TiB/near α Ti matrix composites manufactured by selective laser melting,” Addit. Manuf. 11, pp. 1-4.

[27] Suh N. P., 1973, “The delamination theory of wear,” Wear, 25, pp. 111-124.

[28] Zhang M., Zhang J., McDowell D.L., 2007, “Microstructure-based crystal plasticity modeling of cyclic deformation of Ti–6Al–4V,” Inter. J. of Plasticity, 23, pp. 1328-1348.

[29] Ojha A. and H. Sehitoglu, 2016, “Critical stresses for twinning, slip, and transformation in Ti-based shape memory alloys,” Shap. Mem. Superplasticity 2, pp. 180-195.

[30] Weiss I., Froes F.H., Eylon D., Welsch G. E., 1986, “Modification of alpha morphology in Ti-6Al-4V by thermomechanical processing,” Met. Trans. 11A, 17(11), pp. 1935-1947.

[31] Sabban R., Bahl S., Chatterjee K., Suwas S., 2019, “Globularization using heat treatment in additively manufactured Ti-6Al-4V for high strength and toughness,” Acta Mater. 162, pp. 239-254.

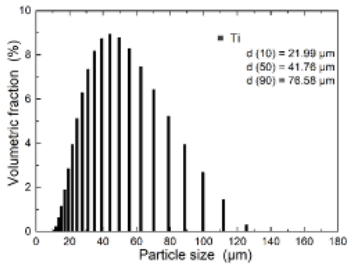

Figure 1 Powder particle size distribution of home-made CP Ti.

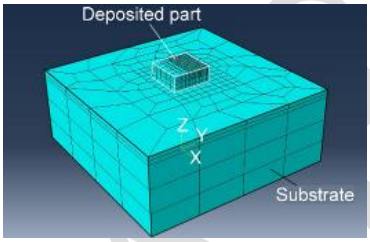

Figure 2 3D finite element analysis (FEA) model of SLM process with CP-Ti (10 layers, 10 laser trace each layer, using optimized process parameters).

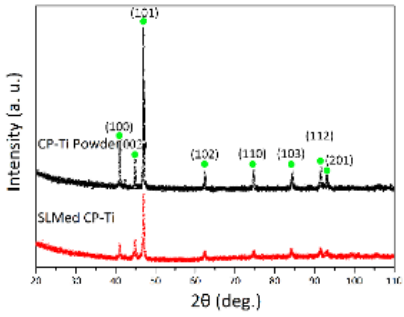

Figure 3 XRD spectra of the CP-Ti powder and SLM-processed specimens (X-ray scanning speed of 1°/min).

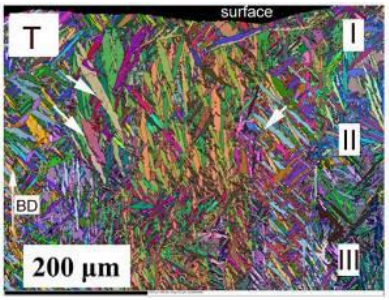

Figure 4 Cross-sectional EBSD measurements All Euler of Regions I, II, and III. (Arrows indicate large-sized lath martensite, BD: building direction).

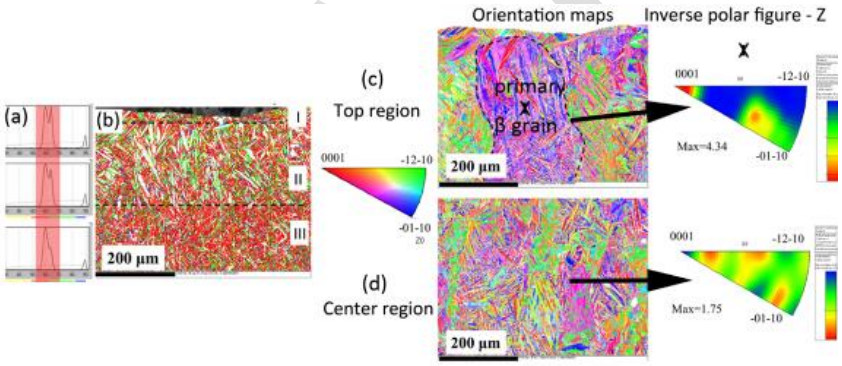

Figure 5 EBSD analyses of SLM processed CP-Ti: (a) grain boundary misorientations associated to (b) grain boundary map; (c,d) inverse polar figures of Regions II and III highlighting texture.

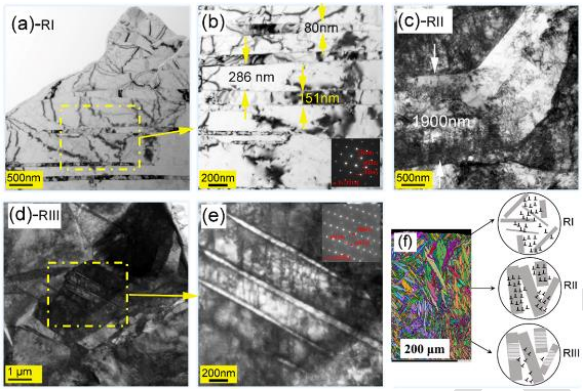

Figure 6 TEM observations of the graded structure in SLM processed CP-Ti specimens: (a, b) Region I, (c) Region II and (d, e) Region III; (f) schematic mechanisms of the heterogeneous in-depth microstructure forming.

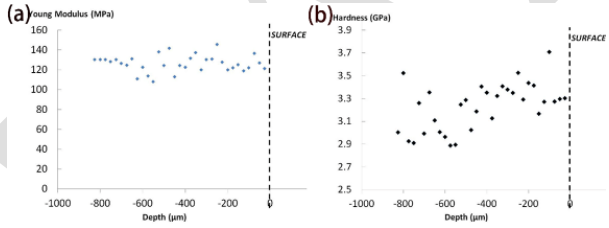

Figure 7 In-depth variations of (a) Young Modulus and (b) Hardness of SLM-processed CP-Ti specimens.

Figure 8 In-depth variations of average COF values and associated advancing behavior (a) of three measurements have been performed at each depth and (b) of stable sliding stage for each measurement.

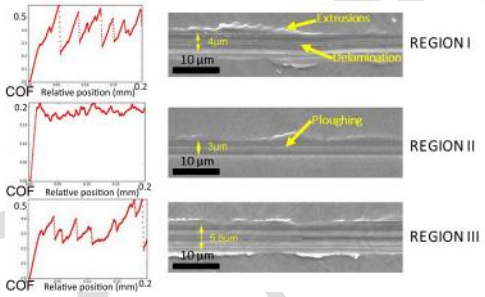

Figure 9 (a) Friction coefficient versus displacement curves representative of the three microstructural Regions and (b) corresponding SEM images showing characteristic morphologies of worn surfaces of SLM-processed CP-Ti specimens.

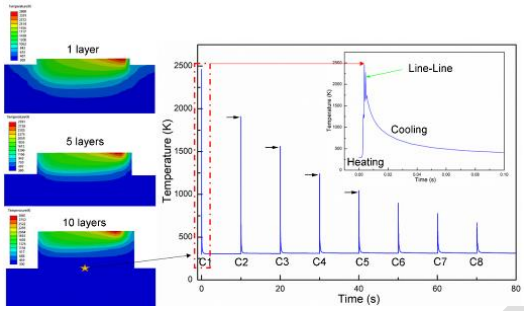

Figure 10 FEA simulation results of thermal field with 1 layer, 5 layers and 10 layers; the thermal cycling during SLM process.

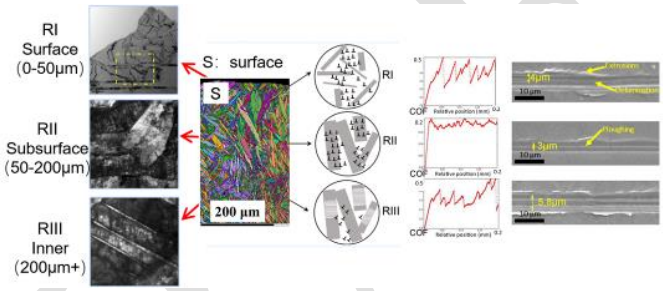

Graphical abstract